

Structure of the connexin 26 gap junction channel at 3.5 Å resolution

Shoji Maeda¹, So Nakagawa¹, Michihiro Suga¹, Eiki Yamashita¹, Atsunori Oshima², Yoshinori Fujiyoshi² & Tomitake Tsukihara^{1,3}

Gap junctions consist of arrays of intercellular channels between adjacent cells that permit the exchange of ions and small molecules. Here we report the crystal structure of the gap junction channel formed by human connexin 26 (Cx26, also known as GJB2) at 3.5 Å resolution, and discuss structural determinants of solute transport through the channel. The density map showed the two membrane-spanning hemichannels and the arrangement of the four transmembrane helices of the six protomers forming each hemichannel. The hemichannels feature a positively charged cytoplasmic entrance, a funnel, a negatively charged transmembrane pathway, and an extracellular cavity. The pore is narrowed at the funnel, which is formed by the six amino-terminal helices lining the wall of the channel, which thus determines the molecular size restriction at the channel entrance. The structure of the Cx26 gap junction channel also has implications for the gating of the channel by the transjunctional voltage.

Intercellular signalling is one of the most essential properties of multicellular organisms. Gap junctions are specialized membrane regions containing hundreds of intercellular communication channels that allow the passage of molecules such as ions, metabolites, nucleotides and small peptides¹. A gap junction channel is formed by end-to-end docking of two hemichannels, also referred to as connexons, each composed of six connexin subunits². Connexin is predicted to have four transmembrane helices and two extracellular loops, which are thought to contain a β -strand structure and are an essential structural basis for the docking of two connexons³. Gap junctions have crucial roles in many biological processes including development, differentiation, cell synchronization, neuronal activity and immune responses^{4,5}. Mutations in connexins thus cause several human diseases, including neurodegenerative diseases, skin diseases, deafness and developmental abnormalities^{5,6}.

To date, more than 20 different connexins have been identified in the human genome, which have been categorized into α , β and γ isoforms on the basis of their sequence homology. The connexin composition of gap junction channels defines their unique properties, such as their selectivity for small molecules, voltage-dependent gating, and response to Ca^{2+} , pH and phosphorylation^{5,7}.

Early electron microscopic analyses of gap junctions suggested that channel gating involves a rotation of all six subunits^{8,9}, and analysis of two-dimensional crystals formed by carboxy-terminally truncated connexin 43 (Cx43, also known as GJA1) resulted in a model for the arrangement of the transmembrane helices and the fold of the connexin protomer^{10,11}. Recently, the electron crystallographic analysis of the connexin 26 Met34Ala mutant (Cx26(M34A)) revealed large densities in the pore at the level of the two membranes, which were interpreted as plugs blocking the channel¹². The structure of Cx26(M34A) was thus assumed to show the channel in a closed state. The structure also suggested that physical blockage by a plug is an essential part of a gating mechanism and is consistent with the physiological studies showing that each connexon can regulate its activity autonomously^{13–15}. Electrophysiological studies have demonstrated that gap junctions have several gating mechanisms.

At least two regulation mechanisms respond to the transjunctional voltage (V_j), V_j gating (fast) and loop gating (slow)¹⁶. Gap junctions can also be gated by the membrane voltage (V_m), termed V_m gating, and by chemical factors such as phosphorylation, pH and Ca^{2+} , known as chemical gating¹⁷.

Here we present an atomic structure of the human Cx26 gap junction channel. We find that the four transmembrane helices of a protomer are arranged differently from the previously proposed pseudoatomic model¹¹, and that several residues associated with non-syndromic hereditary deafness or skin diseases are involved in intra- or intermolecular interactions. We describe in detail the interactions between the two extracellular regions of adjoining connexons. The N-terminal regions of the six subunits line the pore entrance and form a funnel, which restricts the diameter at the entrance of the pore to 14 Å. In conjunction with previous electron microscopy work¹², this finding suggests that conformational changes in the Cx26 N termini play an important part in channel gating, specifically in V_j gating.

Structure determination of the gap junction channel

Structure determination at 3.5 Å is briefly described in the Methods. The whole structure of each protomer—except for residues 110–124 and 218–226 that correspond to most of the cytoplasmic loop and the carboxy-terminal segment, respectively—was successfully modelled in electron density maps. The amino acid assignment was confirmed by methionine sites and disulphide bonds sites (Supplementary Fig. 1). Of the 226 residues of Cx26, the atomic parameters of residues 2–109 and 125–217 converged well during refinement.

The overall structure of the Cx26 gap junction channel, which is formed by two connexons related to each other by a crystallographic two-fold symmetry axis, is similar in shape and size to that of the C-terminal truncated Cx43 gap junction channel visualized by electron crystallography¹⁰ (Fig. 1a). It is a tsuzumi shape, a traditional Japanese drum. The protomers in each hexameric connexon are related by a six-fold non-crystallographic symmetry (NCS) axis perpendicular to the membrane plane (Fig. 1b). The height of the modelled structure of the gap junction channel without disordered cytoplasmic loop and

¹Institute for Protein Research, Osaka University, OLABB, 6-2-3, Furuedai, Suita, Osaka 565-0874, Japan. ²Department of Biophysics, Graduate School of Science, Kyoto University, Oiwake, Kitashirakawa, Sakyo-ku, Kyoto 606-8502, Japan. ³Picobiology Institute, Graduate School of Life Science, University of Hyogo, Kamigohori, Akoh, Hyogo 678-1297, Japan.

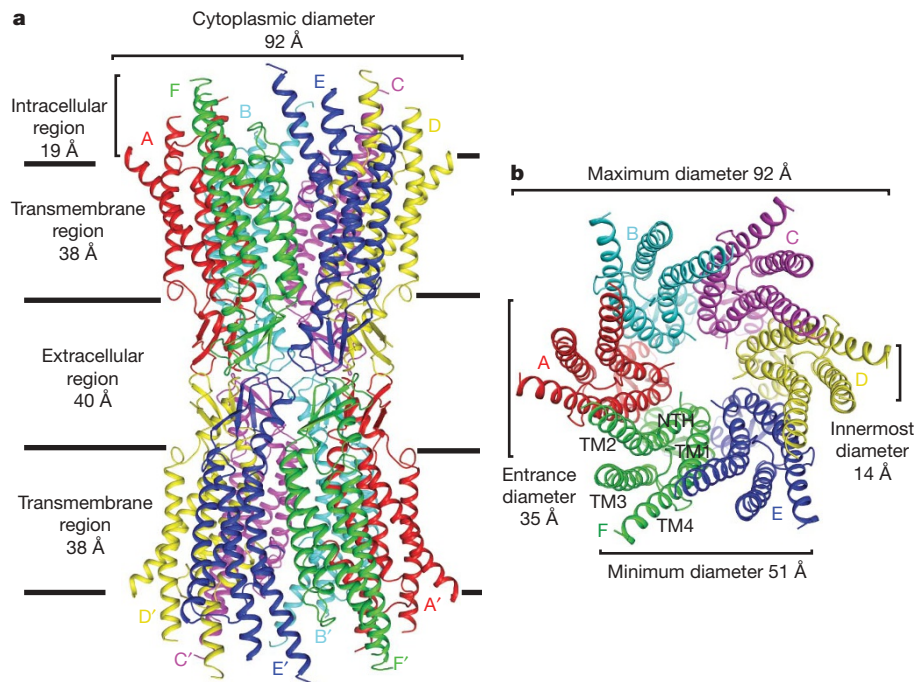


Figure 1 | Overall structure of the Cx26 gap junction channel in ribbon representation. The corresponding protomers in the two hemichannels, which are related by a two-fold axis, are shown in the same colour. **a**, Side view of the Cx26 gap junction channel. **b**, Top view of the Cx26 gap junction

channel showing the arrangement of the transmembrane helices TM1 to TM4. The pore has an inner diameter of 35 Å at the cytoplasmic entrance, and the smallest diameter of the pore is 14 Å.

C-terminal segment is approximately 155 Å. The transmembrane region and membrane surfaces were deduced from the distribution of hydrophobic and aromatic amino acid residues along the non-crystallographic six-fold axis (Fig. 1a and Supplementary Fig. 2). The transmembrane region of the channel is 38 Å thick. TM2 extends about 19 Å from the membrane surface into the cytoplasm. The extracellular region of the connexon extends 23 Å from the membrane surface and interdigitates to the opposite connexon by 6 Å, resulting in the intercellular 'gap' of 40 Å. The extracellular lobes are not protruding so much, as indicated by the structural analyses of split gap junction channels with atomic force microscopy and electron microscopy^{18,19}. The relatively flat lobes could be attributed to the conformational change of the extracellular region induced by the docking of two connexons. The diameter of the connexon is biggest at the cytoplasmic side of the membrane, ~92 Å, and smallest at the extracellular side, ~51 Å. Viewed from the top, the channel looks like a 'hexagonal nut' with a pore in the centre (Fig. 1b). The diameter of the pore is about 40 Å at the cytoplasmic side of the channel, narrowing to 14 Å near the extracellular membrane surface and then widening to 25 Å in the extracellular space. No obvious obstructions are detectable throughout the solute pathway, although this does not exclude the possibility that the cytoplasmic domains not resolved in our map may be able to form a gate. Because the 3.5 Å X-ray structure does not show any obstructions along the pore, our structure of wild-type Cx26 seems to be in an open conformation, which is consistent with the crystallization conditions used (neutral pH without aminosulphonate buffer or any divalent ions).

Structure of the Cx26 protomer

The protomer has four transmembrane segments (TM1–4), two extracellular loops (E1 and E2), a cytoplasmic loop, an N-terminal helix (NTH), and a C-terminal segment (Fig. 2 and Supplementary Fig. 3). Cx26 forms a typical four-helix bundle in which any pair of adjacent helices is antiparallel. TM1 and TM2 face the interior, whereas TM3 and TM4 face the hydrophobic membrane environment. There has been controversy about the identity of the major pore-lining helix, on

the basis of accessibility studies of substituted cysteines and sequence analysis. One set of data favours TM3 as the major pore helix^{11,20} and the other favours TM1 (refs 21, 22). The helical arrangement of our structure is consistent with the latter model. The major pore-lining helix TM1 is inclined, so that the pore diameter narrows from the cytoplasmic to the extracellular side of the membrane, and ends in a short 3_{10} helix (Fig. 2 and Supplementary Fig. 4). TM2 is kinked at Pro 87, the midpoint of the helix, and TM2 and TM3 protrude into the cytoplasm. The Pro87Leu mutation has been shown to cause an aberrant gating²³. Furthermore, mutations of three residues to proline (Leu79Pro, Ser85Pro and Leu90Pro) in TM2 link to deafness²⁴. These mutations probably evoke a structural change in TM2, which would affect the cytoplasmic domains including the NTH. TM4 inclines from the molecular axis by about 30°, generating a larger diameter of the connexon on the intracellular side.

The extracellular loop E1 contains a 3_{10} helix at the beginning and a short α -helix in its C-terminal half (Fig. 2 and Supplementary Fig. 3). E2, together with E1, contains a short antiparallel β -sheet and stretches over E1, forming the outside wall of the connexon. Six conserved cysteine residues, three in each loop, form intramolecular disulphide bonds between E1 and E2 (ref. 3) (Figs 2, 3a and Supplementary Fig. 1). The N-terminal half of E2 seems rather flexible and its amino-acid sequence varies greatly among connexins (Supplementary Fig. 5). The C-terminal half of E2 begins with a 3_{10} turn and is followed by a conserved Pro-Cys-Pro motif that reverses its direction back to TM4.

Most of the prominent intra-protomer interactions are in the extracellular part of the transmembrane region (Fig. 3a and Supplementary Fig. 6). Arg 32 (TM1) interacts with Gln 80 (TM2), Glu 147 (TM3), and Ser 199 (TM4). Two hydrophobic cores around Trp 44 (E1) and Trp 77 (TM2) stabilize the protomer structure. Ala 39 (TM1), Ala 40 (TM1), Val 43 (E1) and Ile 74 (TM2) contribute to the first hydrophobic core around Trp 44, and Phe 154 (TM3) and Met 195 (TM4) form the second core with Trp 77 (Supplementary Fig. 6). In the intracellular part of the transmembrane region, Arg 143 (TM3) forms hydrogen bonds with Asn 206 (TM3) and

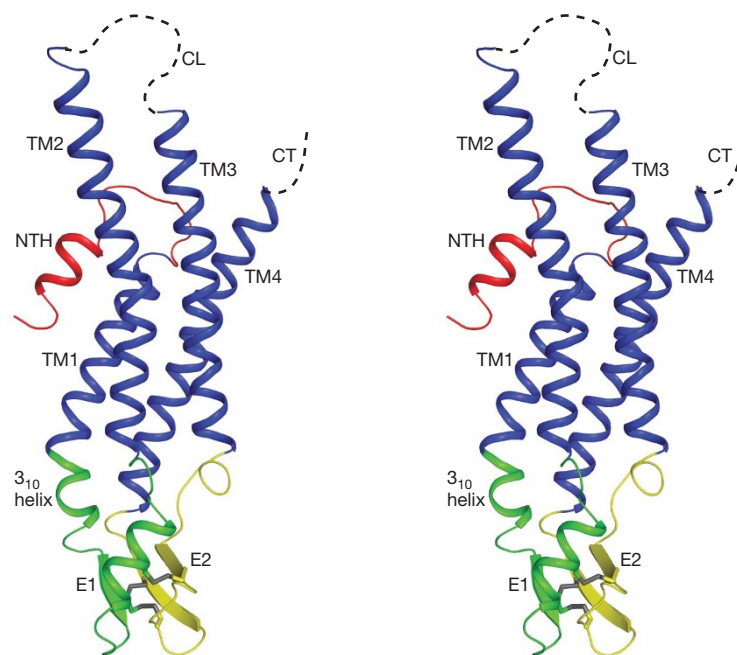


Figure 2 | Stereo view of the Cx26 protomer in ribbon representation. Colour code: red, NTH; blue, TM1–TM4; green, E1; yellow, E2; grey, disulphide bonds; dashed lines, cytoplasmic loop (CL) and C terminus (CT),

Ser 139 (TM3) (Supplementary Fig. 6). The four-helix bundle is further stabilized by dipole–dipole interactions of the antiparallel helices²⁵.

Structural organization of the hexameric connexon

The inter-protomer interactions in the hexameric connexon are mostly located in the extracellular half of transmembrane helices TM2 and TM4 and in the extracellular loops. Glu 47 (E1), Gln 48 (E1), Asn 62 (E1), Asp 66 (E1), Tyr 65 (E1), Arg 75 (TM2) and the main-chain amide of Ser 72 (E1) from one protomer, and

which were not visible in the map. E1 and E2 are the loops connecting TM1 and TM2, and TM3 and TM4, respectively.

Asp 46 (E1), Asp 50 (E1), Arg 184 (E2) Thr 186 (TM4) and Glu 187 (TM4) from the adjacent protomer form the core of the inter-protomer interactions (Supplementary Fig. 7). Although TM3 is evolutionarily more variable than the other three helices, every third or fourth residue in TM3 is aromatic, generating an aromatic face that is conserved among connexins. Each helix in a protomer contributes to an aromatic cluster in the groove between two adjacent protomers (Supplementary Fig. 7). Most of the residues involved in intra- and inter-protomer interactions are conserved

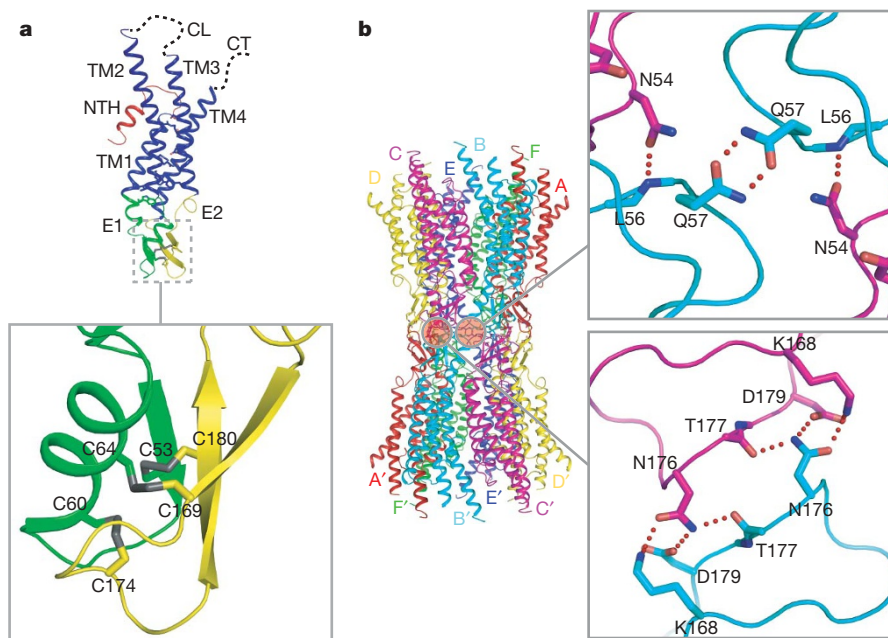


Figure 3 | Molecular architecture of the Cx26 gap junction channel. The C α trace is shown in ribbon or line representation and the side chains in the close-up views in the boxes are shown as sticks. Hydrogen bonds or salt bridges are shown as dotted lines. **a**, Disulphide bonds between two

extracellular loops in the Cx26 protomer. **b**, Intercellular interactions. The protomers forming the gap junction channel are labelled A to F and A' to F' each in the same colour as in Fig. 2. The right top and bottom boxes show intercellular interactions in E1 and E2, respectively.

within the connexin family (Supplementary Fig. 5), and mutations of these residues are associated with deafness and skin diseases²⁴. The mutations probably interfere with the proper folding and/or oligomerization of connexins, thus resulting in defective channels.

Architectures of the intercellular junction and channel

Our structure revealed the interactions between the two adjoining connexons of the gap junction channel, which involve both E1 and E2 (Fig. 3b). In E1, Asn 54 forms hydrogen bonds with the main-chain amide of Leu 56 in the opposite protomer, and Gln 57 forms symmetric hydrogen bonds with the same residue of the diagonally opposite protomer. These residues are highly conserved among connexins (Supplementary Fig. 5). In E2, Lys 168, Asp 179 and the main-chain carbonyl groups of Thr 177 and Asn 176 form hydrogen bonds and salt bridges with the opposite protomer. Together with interactions between the protomers in the two hemichannels, these interactions create a tight double-layered wall bridging the extracellular gap, which connects the two adjoining hemichannels and separates the channel interior from the extracellular environment.

The permeation pathway of a gap junction channel consists of an intracellular channel entrance, a pore funnel and an extracellular cavity. The intracellular channel entrance has a diameter of 40 Å and is formed by the intracellular parts of TM2 and TM3. Eleven positively charged residues, nine in TM2 and two in TM3, generate a positively charged environment at the channel entrance (Fig. 4a). The positive atmosphere around the intracellular channel entrance would be favourable for concentrating and increasing absolute permeability of negatively charged molecules²⁶.

The funnel surface is lined by N-terminal residues Asp 2, Trp 3, Thr 5, Leu 6 and Ile 9 (Fig. 4b). Most α -connexins have a conserved Phe residue at the position of Thr 5 in Cx26, except for Cx43, which has an Ala residue (Supplementary Fig. 8). Because the funnel forms a constriction site at the cytoplasmic entrance of the pore, the size and electrical character of the side chains in this region should have a strong effect on both the molecular cutoff size and the charge selectivity of the channel. In line with this notion, it has previously been reported that the charges in the N-terminal region have a crucial involvement in

determining the charge selectivity of the channel²⁷. Cx43 channels are known to have the widest functional pore, followed by β -connexins and then other α -connexins^{26,28}, which could be reasonably derived from the size of the side chain at the position 5.

Twelve copies of the N-terminal half of E1 form the inner wall of the extracellular cavity of the pore, which has dimensions of $25 \times 25 \times 30 \text{ Å}^3$ (Fig. 4a, b). This finding is in agreement with a functional study that demonstrated that E1 lines the pore in the extracellular gap region²⁹. The pore-lining residues at the TM1/E1 boundary are Lys 41, Glu 42 and Gly 45. Lys 41 creates a narrowed part of the pore with the diameter of about 17 Å and is unique to Cx26 (Supplementary Fig. 8), generating a more positively charged environment between the funnel and the following negatively charged part of the solute pathway. The TM1/E1 boundary has been suggested to be involved in voltage sensing, together with the N terminus¹⁴. Although there is no direct interaction between Lys 41 and the N terminus of Cx26 (the distance between Lys 41 and the bottom of the funnel is approximately 8 Å), it is conceivable that Lys 41 and the Cx26-specific N terminus act together in sensing the voltage field. Asp 46 and Asp 50, highly conserved residues in the connexin family (Supplementary Fig. 8), face the pore interior and create a 9-Å long, negatively charged path with a diameter of 20 Å, approximately at the height of the extracellular membrane surface (Fig. 4a). Along with the pore funnel, these two regions probably contribute to the size restriction and possibly to the charge selectivity, considering the pore diameter and the charge character.

Pore funnel and the voltage-dependent gating mechanism

The short NTHs of the six protomers form the funnel (Fig. 5), and their very high crystallographic temperature factors indicate that these are the most mobile domains in the structure (Supplementary Fig. 9a, b). This finding agrees with an NMR solution structure of an N-terminal peptide of Cx26, which showed that the loop connecting the NTH to TM1 is very flexible³⁰. Asp 2 forms hydrogen bonds with the main-chain amide of Thr 5 from the neighbouring protomer. The Asp 2 and Thr 5 residues on neighbouring NTHs at the bottom of the funnel form a circular girdle, as previously seen in the nicotinic acetylcholine receptor³¹, which stabilizes the funnel structure (Fig. 5). Trp 3 forms

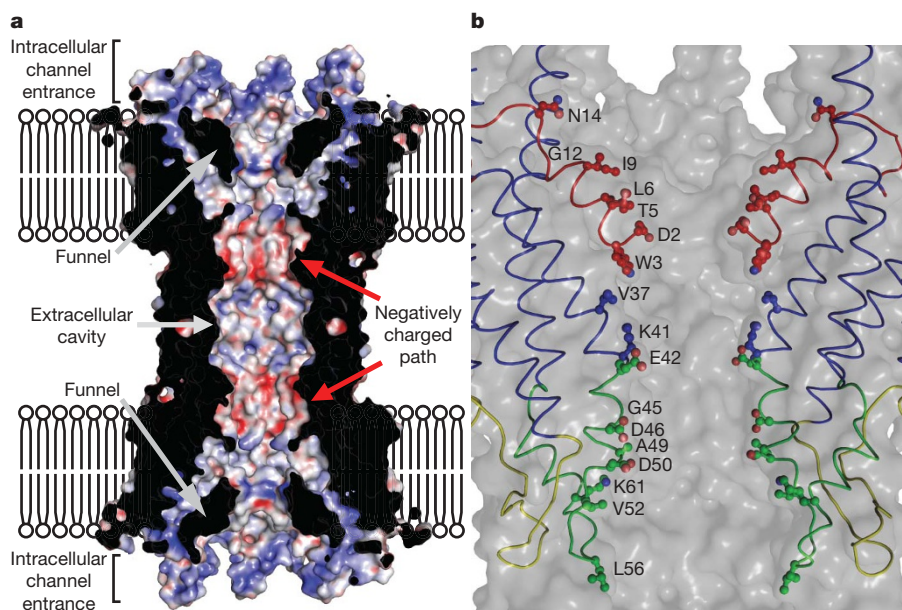


Figure 4 | Pore structure of the Cx26 gap junction channel. **a**, Vertical cross-section through the gap junction channel, showing the surface potential inside the channel. The channel features a wide cytoplasmic opening, which is restricted by the funnel structure, a negatively charged path and an extracellular cavity at the middle. Electrostatic surface potential of the Cx26 gap junction channel was calculated by the program APBS⁴³ as implemented in PyMOL under dielectric constants of 2.0 and 80.0 for

protein and solvent regions, respectively. The displayed potentials range from -40 (red) to 40 (blue) $kT e^{-1}$. **b**, Pore-lining residues in a Cx26 gap junction channel. Side view of Cx26 gap junction channel pore; the main chain is depicted as a thin ribbon and side chains facing the pore as balls and sticks. For fine viewing, two subunits in the foreground are omitted in the surface representation and two further subunits in the background are omitted in the model depiction. The colouring is the same as in Fig. 3b.

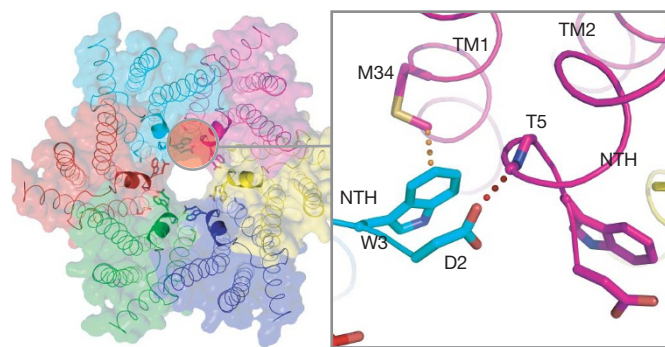


Figure 5 | Structure of the pore funnel. The six NTHs form a funnel structure, which is stabilized by a circular network of hydrogen bonds between Asp 2 and the main chain of Thr 5. The Cx26 protomers are shown in line and the NTHs in ribbon representation superposed on a surface representation. The close-up view shows the interaction between the indole ring of Trp 3 and the methyl group of Met 34 (TM1) in the adjacent protomer (hydrophobic interaction: orange broken line; hydrogen bond: red broken line).

hydrophobic interactions with Met 34 (TM1) of the neighbouring protomer, which draws the NTH to the inner wall of the channel. This interaction maintains the funnel in the open state, with an inner diameter of 14 Å. One of the most frequent deafness mutations is Met34Thr, which decreases electrical current, but forms structures indistinguishable from wild-type gap junctions^{32,33}. This mutation would indeed disrupt the interaction of the NTH with Trp 3, which would cause the funnel to detach from the inner wall of the pore, resulting in a narrower funnel. This concept is supported by recent electron microscopy studies that showed a prominent density in the centre of the pore in Cx26(Met34Ala)¹², which was decreased in the N-terminal deletion mutant Cx26(Met34Ala-del2–7)³⁴.

Cx26 channels are known to be closed by an inside positive potential¹⁴. This is opposite from the gating property of Cx32, which has Asn at position 2 and closes after an inside negative potential¹⁴. A cytoplasmic movement of the N-terminal portion, where the voltage sensor is believed to reside, has been suggested to initiate voltage-dependent gating^{14,35,36}. The recent electron microscopy structure of the Met34Ala mutant of Cx26 shows a plug that blocks the pore¹², which may be due to the smaller side chain at position 34 causing the channel to adopt a closed conformation. Although this electron microscopy structure may not exactly represent a physiological closed state, it is conceivable that an inside positive V_j would cause an inward movement of Asp 2, thus preventing the interactions between Asp 2–Trp 5 and Trp 3–Met 34, which could function as a trigger for gating in response to a change in V_j . The released NTHs could then assemble into a plug that physically blocks the pore. The NTHs would not be released by the opposite potential, because they would be kept in position by their interaction with Met 34 (Supplementary Fig. 10). The release of any one of the six NTH would break down or destabilize the circular hydrogen bond network through the Asp 2–Thr 5 girdle, resulting in subconductance states of the channel. This would account for the report that the conformational change of a single subunit is sufficient to initiate V_j gating³⁷, although it is unclear whether the other five N termini adopt the same conformation as the one in action. In this way, the heteromeric oligomerization in a connexon would enable bipolar V_j gating³⁷, which allows the characteristic regulation of channel activity depending on the connexin isoforms expressed in each tissue.

The structure in this work could suggest a speculative V_j -gating model, in which the N termini have the chief role in sensing V_j within the conductive pore and in forming the plug to close the pore. This model is not the case for other voltage-sensitive ion channels containing the S4 helix as a voltage sensor³⁸, but is in accord with previous physiological studies^{13,35,36}. However, we should consider an alternative

possibility, because connexins are thought to use several gating mechanisms^{39,40} and the previous electron microscopy structure was analysed in the condition that facilitates closure by chemical gating¹². The C terminus of Cx26 is thought to be too short to form the gating particle suggested for Cx43 (ref. 41), but it is still associated with the chemical regulation of channel activity¹². The structure in this work strongly suggests that the plug detected in the electron microscopy structure is composed of the assembly of Cx26 N termini. However, we do not rule out the possibility that the invisible cytoplasmic loop or the C terminus might contribute as a component. At present it is too premature to address the mechanism related to chemical gating from our structure.

Further discussions on the roles of the N terminus, the cytoplasmic loop and the C terminus are given in Supplementary Discussion.

METHODS SUMMARY

Human Cx26 was expressed in Sf9 insect cells using recombinant baculovirus. The gap junction channel was solubilized in dodecylmaltoside and purified sequentially by cation exchange and size-exclusion chromatography. Crystals were grown by the hanging-drop vapour diffusion method with PEG200 as a precipitant. The structure was determined by the single-isomorphous replacement combined with anomalous scattering (SIRAS) method, with phase extension by six-fold non-crystallographic (NCS) averaging.

Full Methods and any associated references are available in the online version of the paper at www.nature.com/nature.

Received 9 October 2008; accepted 9 February 2009.

- Kumar, N. M. & Gilula, N. B. The gap junction communication channel. *Cell* **84**, 381–388 (1996).
- Harris, A. L. Emerging issues of connexin channels: biophysics fills the gap. *Q. Rev. Biophys.* **34**, 325–472 (2001).
- Foot, C. I., Zhou, L., Zhu, X. & Nicholson, B. J. The pattern of disulfide linkages in the extracellular loop regions of connexin 32 suggests a model for the docking interface of gap junctions. *J. Cell Biol.* **140**, 1187–1197 (1998).
- Levin, M. Gap junctional communication in morphogenesis. *Prog. Biophys. Mol. Biol.* **94**, 186–206 (2007).
- Saez, J. C., Berthoud, V. M., Branes, M. C., Martinez, A. D. & Beyer, E. C. Plasma membrane channels formed by connexins: their regulation and functions. *Physiol. Rev.* **83**, 1359–1400 (2003).
- Kelsell, D. P., Dunlop, J. & Hodgins, M. B. Human diseases: clues to cracking the connexin code? *Trends Cell Biol.* **11**, 2–6 (2001).
- Simon, A. M. & Goodenough, D. A. Diverse functions of vertebrate gap junctions. *Trends Cell Biol.* **8**, 477–483 (1998).
- Unwin, P. N. & Zampighi, G. Structure of the junction between communicating cells. *Nature* **283**, 545–549 (1980).
- Unwin, P. N. & Ennis, P. D. Two configurations of a channel-forming membrane protein. *Nature* **307**, 609–613 (1984).
- Unger, V. M., Kumar, N. M., Gilula, N. B. & Yeager, M. Three-dimensional structure of a recombinant gap junction membrane channel. *Science* **283**, 1176–1180 (1999).
- Fleishman, S. J., Unger, V. M., Yeager, M. & Ben-Tal, N. A C- α model for the transmembrane α helices of gap junction intercellular channels. *Mol. Cell* **15**, 879–888 (2004).
- Oshima, A., Tani, K., Hiroaki, Y., Fujiyoshi, Y. & Sosinsky, G. E. Three-dimensional structure of a human connexin26 gap junction channel reveals a plug in the vestibule. *Proc. Natl Acad. Sci. USA* **104**, 10034–10039 (2007).
- Harris, A. L., Spray, D. C. & Bennett, M. V. Kinetic properties of a voltage-dependent junctional conductance. *J. Gen. Physiol.* **77**, 95–117 (1981).
- Verselis, V. K., Ginter, C. S. & Bargiello, T. A. Opposite voltage gating polarities of two closely related connexins. *Nature* **368**, 348–351 (1994).
- Ebihara, L., Berthoud, V. M. & Beyer, E. C. Distinct behavior of connexin56 and connexin46 gap junctional channels can be predicted from the behavior of their hemi-gap-junctional channels. *Biophys. J.* **68**, 1796–1803 (1995).
- Bukauskas, F. F., Bukauskiene, A., Bennett, M. V. & Verselis, V. K. Gating properties of gap junction channels assembled from connexin 43 and connexin 43 fused with green fluorescent protein. *Biophys. J.* **81**, 137–152 (2001).
- Bukauskas, F. F. & Verselis, V. K. Gap junction channel gating. *Biochim. Biophys. Acta* **1662**, 42–60 (2004).
- Muller, D. J., Hand, G. M., Engel, A. & Sosinsky, G. E. Conformational changes in surface structures of isolated connexin 26 gap junctions. *EMBO J.* **21**, 3598–3607 (2002).
- Perkins, G. A., Goodenough, D. A. & Sosinsky, G. E. Formation of the gap junction intercellular channel requires a 30° rotation for interdigitating two apposing connexons. *J. Mol. Biol.* **277**, 171–177 (1998).
- Skerrett, I. M. et al. Identification of amino acid residues lining the pore of a gap junction channel. *J. Cell Biol.* **159**, 349–360 (2002).

21. Zhou, X. W. *et al.* Identification of a pore lining segment in gap junction hemichannels. *Biophys. J.* **72**, 1946–1953 (1997).
22. Kronengold, J., Trexler, E. B., Bukauskas, F. F., Bargiello, T. A. & Verselis, V. K. Single-channel SCAM identifies pore-lining residues in the first extracellular loop and first transmembrane domains of Cx46 hemichannels. *J. Gen. Physiol.* **122**, 389–405 (2003).
23. Suchyna, T. M., Xu, L. X., Gao, F., Fournier, C. R. & Nicholson, B. J. Identification of a proline residue as a transduction element involved in voltage gating of gap junctions. *Nature* **365**, 847–849 (1993).
24. Laird, D. W. Life cycle of connexins in health and disease. *Biochem. J.* **394**, 527–543 (2006).
25. Sheridan, R. P., Levy, R. M. & Salemme, F. R. α -helix dipole model and electrostatic stabilization of 4- α -helical proteins. *Proc. Natl Acad. Sci. USA* **79**, 4545–4549 (1982).
26. Weber, P. A., Chang, H. C., Spaeth, K. E., Nitsche, J. M. & Nicholson, B. J. The permeability of gap junction channels to probes of different size is dependent on connexin composition and permeant-pore affinities. *Biophys. J.* **87**, 958–973 (2004).
27. Oh, S., Verselis, V. K. & Bargiello, T. A. Charges dispersed over the permeation pathway determine the charge selectivity and conductance of a Cx32 chimeric hemichannel. *J. Physiol. (Lond.)* **586**, 2445–2461 (2008).
28. Gong, X. Q. & Nicholson, B. J. Size selectivity between gap junction channels composed of different connexins. *Cell Commun. Adhes.* **8**, 187–192 (2001).
29. Trexler, E. B., Bukauskas, F. F., Kronengold, J., Bargiello, T. A. & Verselis, V. K. The first extracellular loop domain is a major determinant of charge selectivity in connexin46 channels. *Biophys. J.* **79**, 3036–3051 (2000).
30. Purnick, P. E., Benjamin, D. C., Verselis, V. K., Bargiello, T. A. & Dowd, T. L. Structure of the amino terminus of a gap junction protein. *Arch. Biochem. Biophys.* **381**, 181–190 (2000).
31. Miyazawa, A., Fujiyoshi, Y. & Unwin, N. Structure and gating mechanism of the acetylcholine receptor pore. *Nature* **423**, 949–955 (2003).
32. Kelsell, D. P. *et al.* Connexin 26 mutations in hereditary non-syndromic sensorineural deafness. *Nature* **387**, 80–83 (1997).
33. Oshima, A., Doi, T., Mitsuoaka, K., Maeda, S. & Fujiyoshi, Y. Roles of Met-34, Cys-64, and Arg-75 in the assembly of human connexin 26. Implication for key amino acid residues for channel formation and function. *J. Biol. Chem.* **278**, 1807–1816 (2003).
34. Oshima, A., Tani, K., Hiroaki, Y., Fujiyoshi, Y. & Sosinsky, G. E. Projection structure of a N-terminal deletion mutant of connexin 26 channel with decreased central pore density. *Cell Commun. Adhes.* **15**, 85–93 (2008).
35. Purnick, P. E., Oh, S., Abrams, C. K., Verselis, V. K. & Bargiello, T. A. Reversal of the gating polarity of gap junctions by negative charge substitutions in the N-terminus of connexin 32. *Biophys. J.* **79**, 2403–2415 (2000).
36. Oh, S., Rivkin, S., Tang, Q., Verselis, V. K. & Bargiello, T. A. Determinants of gating polarity of a connexin 32 hemichannel. *Biophys. J.* **87**, 912–928 (2004).
37. Oh, S., Abrams, C. K., Verselis, V. K. & Bargiello, T. A. Stoichiometry of transjunctional voltage-gating polarity reversal by a negative charge substitution in the amino terminus of a connexin 32 chimera. *J. Gen. Physiol.* **116**, 13–31 (2000).
38. Jan, L. Y. & Jan, Y. N. Structural elements involved in specific K⁺ channel functions. *Annu. Rev. Physiol.* **54**, 537–555 (1992).
39. Trexler, E. B., Bennett, M. V. L., Bargiello, T. A. & Verselis, V. K. Voltage gating and permeation in a gap junction hemichannel. *Proc. Natl Acad. Sci. USA* **93**, 5836–5841 (1996).
40. Peracchia, C. Chemical gating of gap junction channels; roles of calcium, pH and calmodulin. *Biochim. Biophys. Acta* **1662**, 61–80 (2004).
41. Delmar, M., Coombs, W., Sorgen, P., Duffy, H. S. & Taffet, S. M. Structural bases for the chemical regulation of connexin43 channels. *Cardiovasc. Res.* **62**, 268–275 (2004).
42. Tao, L. & Harris, A. L. 2-Aminoethoxydiphenyl borate directly inhibits channels composed of connexin26 and/or connexin32. *Mol. Pharmacol.* **71**, 570–579 (2007).
43. Baker, N. A., Sept, D., Joseph, S. & Holst, M. J. McCammon, J. A. Electrostatics of nanosystems: applications to microtubules and the ribosomes. *Proc. Natl Acad. Sci. USA* **98**, 10037–10041 (2001).

Supplementary Information is linked to the online version of the paper at www.nature.com/nature.

Acknowledgements We thank T. Tomizaki for help in the diffraction data collection on X06SA at the Swiss Light Source. This work was supported by Grants-in-Aid for Scientific Research (10687101, 16087206 and 18207006) and the GCOE program (A-041) from the Ministry of Education, Culture, Sports, Science, and Technology of Japan (to T.T.), the Japan Biological Informatics Consortium (to T.T.), the Strategic Japan-UK Cooperation Program of the Japan Science and Technology Agency (to T.T.), and Grants-in-Aid for Specially Promoted Research (to Y.F.) and the New Energy and Industrial Technology Development Organization (to Y.F.). We thank T. Walz for critical reading of this manuscript.

Author Contributions S.M., S.N., M.S., E.Y. and T.T. performed X-ray structural analysis. S.M., A.O., Y.F. and T.T. wrote the paper.

Author Information The atomic coordinate and the structure factor for the reported crystal structure have been deposited with the Protein Data Bank under accession code 2ZW3. Reprints and permissions information is available at www.nature.com/reprints. Correspondence and requests for materials should be addressed to T.T. (tsuki@protein.osaka-u.ac.jp).

METHODS

Expression and purification of Cx26. The human Cx26 complementary DNA was amplified from a human liver cDNA library (Human liver QUICK-Clone cDNA, Clontech) by PCR and inserted via BamHI/EcoRI restriction sites into a pBlueBac4.5 (Invitrogen) baculovirus transfer vector. Recombinant baculovirus was made using the Bac-N-Blue system (Invitrogen). Baculovirus-infected Sf9 cells were grown at 27–28 °C and collected three days after infection. Purified Cx26 was obtained according to previously described and slightly modified methods⁴⁴. In brief, collected cells were disrupted in alkali buffer containing 20 mM NaOH, 1 mM EDTA, 1 mM EGTA and 2 mM dithiothreitol (DTT), followed by ultracentrifugation to isolate the purified gap junction membrane fraction. The membrane fraction was then solubilized with 1–1.5% *n*-dodecyl- β -D-maltoside (DDM) in 10 mM CAPS (pH 10.5), 1 M NaCl and 10 mM DTT. The resulting supernatant was mixed with cation exchange resin, and Cx26 was eluted in 10 mM HEPES (pH 7.5), 0.01% DDM, 2 mM DTT and 500–1,000 mM NaCl. The protein was further purified by size-exclusion chromatography in 10 mM HEPES (pH 7.5), 200 mM NaCl, 2 mM DTT, 0.01% *n*-undecyl- β -D-maltoside (UDM), concentrated to 30 mg ml⁻¹, and used for crystallization. To prepare seleno-methionine (SeMet)-labelled protein⁴⁵, Sf9 cells were collected by centrifugation 24 h after infection, washed with sterilized PBS and transferred into medium devoid of methionine and supplemented with 20 mg l⁻¹ SeMet and 150 mg l⁻¹ L-cysteine. After a 4-h incubation, the cells were collected by centrifugation and transferred into medium supplemented with 50 mg l⁻¹ SeMet and 150 mg l⁻¹ L-cysteine. The cells were collected after two days, and SeMet-labelled protein was purified using the same protocol as for native protein.

Crystallization. Crystals were obtained by vapour diffusion (4 °C) by mixing equal volumes of protein solution and reservoir solution containing 100 mM potassium phosphate (pH 7.5), 100 mM KCl, 10 mM DTT, 0.5 mM EGTA and 16–18% PEG200. Crystals were dehydrated by gradually adding triethyleneglycol to a final concentration of 25–30% and flash frozen in liquid nitrogen. The Ta₆Br₁₄ derivative was prepared by soaking the crystals in 1 mM Ta₆Br₁₄ overnight.

X-ray data collection. Data sets were collected on BL44XU at Spring-8 with a DIP6040 imaging-plate detector (Bruker AXS). Two non-isomorphous native data sets, Native I and Native II, were collected at 3.5 Å and 4.0 Å, respectively. Isomorphous derivative crystals were generated for each native crystal (Derivative I, and Derivative II). Three data sets of tantalum derivative crystals were acquired by tuning X-rays at 0.9000 Å (remote), 1.2526 Å (peak), and 1.2552 Å (edge) (Derivative III). Diffraction data for the crystals, Native I, Native II and Derivative II were acquired with X-rays of 0.9000 Å, and that of Derivative I were acquired with X-rays of 1.2526 Å. Diffraction data of SeMet derivative crystals were collected with X-rays of 0.9000 Å (remote) and 0.9790 Å (edge). Another diffraction data set was acquired on the X06SA beamline at the Swiss Light Source, Paul Scherrer Institute, Villigen, Switzerland, using 1.7000 Å X-rays to detect anomalous dispersion effects of sulphur atoms in the native crystal using a Pilatus 6M detector. All X-ray experiments were performed at 100 K. The Spring-8 diffraction data were processed and scaled with the Denzo, Scalepack⁴⁶ and CCP4 programs⁴⁷. The SLS data were processed and scaled with the XDS and XSCALE programs⁴⁸. The native crystals belonged to the space group C2 with cell dimensions of *a* = 167.6 Å, *b* = 111.2 Å, *c* = 155.4 Å and β = 114.0. Experimental conditions and statistics of intensity data acquisition are given in Supplementary Table 1.

Structure determination. Rotation function calculation of native crystals performed by POLARREF⁴⁷ indicated a six-fold axis perpendicular to the crystallographic two-fold axis. The sites of the Ta₆Br₁₄ clusters were determined in the difference Patterson map calculated with Native I data and Derivative III (remote) data at 6 Å resolution. Derivative III (peak) data were included in the phase determination, and anomalous dispersion effects of the heavy atoms were taken into account for the phase estimation. Assuming the tantalum cluster to be a single atom, the positional parameters and B-factor of the tantalum cluster were refined with the program SHARP⁴⁹. Because of its large size, the tantalum cluster was effective for phase determination to no more than 6 Å resolution. The phases were refined and extended to 3.5 Å resolution by NCS averaging and solvent flattening using the program DM⁵⁰. The preliminarily refined phase set was used to calculate a difference Fourier map of the SeMet derivative with coefficients of $[F_o(\text{remote}) - F_o(\text{edge})] \times \exp(i\alpha_c)$, in which α_c is the preliminarily refined phase. The SeMet sites were determined in the difference Fourier map. Of 42 methionine sites in the protein molecule, 36 were identified by selenium peaks higher than 4 σ in the electron density distribution in the anomalous difference Fourier map. Thirty sites were used for phase calculations, whereas the other six sites were used to monitor the phase improvement steps.

Two native crystals, a tantalum derivative crystal, and a SeMet replacement crystal were used for the phase refinement by the multi-crystal averaging. Initial

phases of each data set for the phase refinement were determined at 6 Å or 7 Å resolution. Those of the Native I crystal were determined by the SIRAS method using the Derivative I data at 6 Å resolution. Those of the Native II crystal equilibrated with 25% triethyleneglycol were determined by the single isomorphous replacement (SIR) method using the Derivative II data at 7 Å resolution. Those of the tantalum derivative crystal were determined by the Multiplexed anomalous dispersion (MAD) method using the Derivative III remote, peak, and edge data at 6 Å resolution. Those of the SeMet replacement crystal were determined by a method equivalent to the SIR method using the SeMet edge and remote data at 6 Å resolution.

The phase refinement was performed by multi-crystal averaging and six-fold NCS averaging combined with solvent flattening with the program DMULTI⁵¹. The refinement procedure was monitored by *R* and *C* factors as a measure of consistency between observed and calculated structure factors, F_o and F_c , in which $R = \sum |F_o - F_c| / \sum |F_o|$, $C = \sum (F_o - \langle F_o \rangle) (F_c - \langle F_c \rangle) / \sum [(F_o - \langle F_o \rangle)^2 (F_c - \langle F_c \rangle)^2]^{1/2}$, and $\langle F_o \rangle$ and $\langle F_c \rangle$ are the averaged values of F_o and F_c in each resolution range. The phases were extended to 3.5 Å resolution, and the refinement converged well, with *R* = 0.262 and *C* = 0.891. An electron density map was calculated with the observed structure factors of Native I and the refined phases. The electron density map is called SIRAS/DM map in this paper.

Model building was performed using the programs O⁵² and coot⁵³, and structural refinement was carried out under a tight restraint of non-crystallographic six-fold symmetry with the programs Crystallographic and NMR System (CNS)⁵⁴ and REFMAC⁵⁵. The backbone of the protein was successfully traced in the SIRAS/DM map and in the composite omit map, in which aromatic residues are seen as bulky electron density (Supplementary Fig. 11a, b). To determine SeMet sites, a difference Fourier map was calculated at 6 Å resolution with coefficients of $[F_o(\text{remote}) - F_o(\text{edge})] \exp(i\alpha)$, in which $F_o(\text{remote})$ and $F_o(\text{edge})$ are the observed structure factors of the SeMet derivative measured by X-rays of 0.9000 Å and 0.9790 Å, and α is the phase of the Native I crystal determined by the SIR method with Ta derivative I combined with NCS averaging. The electron density of the Se atom at the N terminus was not detected in the difference map, probably due to disordered structure. To confirm the locations of the three disulphide bonds, which are close to each other, a native anomalous difference Fourier map was calculated at 4 Å resolution with the native F_o data acquired at the SLS and the phases calculated from a structural model refined by replacing their cysteine residues with alanine residues.

Crystallographic *R* and *R*_{free} for 5% of the reflections excluded from the refinement were calculated to monitor the structural refinement procedures. The close values of the final *R* and *R*_{free} were caused by the six-fold NCS restraints applied in the refinement⁵⁶. The results of the structural analysis are summarized in Supplementary Table 1. The final *R* and *R*_{free} values were 33.7% and 35.1%, respectively. The main-chain dihedral angles for 84.0% of the non-glycine residues were in the most favoured region of the Ramachandran plot, 15.5% were in the allowed region, 0.5% were in the generously allowed region, and no residues were in the disallowed region. The refined structure was validated using the program PROCHECK⁵⁷. All molecular graphics were created with Pymol⁵⁸.

44. Stauffer, K. A., Kumar, N. M., Gilula, N. B. & Unwin, N. Isolation and purification of gap junction channels. *J. Cell Biol.* **115**, 141–150 (1991).
45. Bellizzi, J. J. III, Widom, J., Kemp, C. W. & Clardy, J. Producing selenomethionine-labeled proteins with a baculovirus expression vector system. *Structure* **7**, R263–R267 (1999).
46. Otwinowski, Z. & Minor, W. Processing of X-ray diffraction data collected in oscillation mode. *Methods Enzymol.* **276**, 307–326 (1997).
47. Collaborative Computational Project 4. The CCP4 suite: Programs for Protein Crystallography. *Acta Crystallogr. D* **50**, 760–763 (1994).
48. Kabsch, W. Automatic processing of rotation diffraction data from crystals of initially unknown symmetry and cell constants. *J. Appl. Cryst.* **26**, 795–800 (1993).
49. Bricogne, G., Vonrhein, C., Flensburg, C., Schiltz, M. & Paciorek, W. Generation, representation and flow of phase information in structure determination: recent developments in and around SHARP 2.0. *Acta Crystallogr. D* **59**, 2023–2030 (2003).
50. Cowtan, K. An automated procedure for phase improvement by density modification. *Joint CCP4 ESF-EACBM Newsletter Protein Crystallogr.* **31**, 34–38 (1994).
51. Cowtan, K. D. & Zhang, K. Y. Density modification for macromolecular phase improvement. *Prog. Biophys. Mol. Biol.* **72**, 245–270 (1999).
52. Jones, T. A., Zou, J. Y. & Cowan, S. W. Improved methods for building protein models in electron density maps and the location of errors in these models. *Acta Crystallogr. A* **47**, 110–119 (1991).
53. Emsley, P., Cowtan, K. Coot: model-building tools for molecular graphics. *Acta Crystallogr. D* **60**, 2126–2132 (2004).
54. Brunger, A. T. et al. Crystallography and NMR system: A new software suite for macromolecular structure determination. *Acta Crystallogr. D* **54**, 905–921 (1998).

55. Murshudov, G. N., Vagin, A. A. & Dodson, E. J. Refinement of macromolecular structures by the maximum-likelihood method. *Acta Crystallogr. D* **53**, 240–255 (1997).
56. Dodson, E., Kleywegt, G. J. & Wilson, K. Report of a workshop on the use of statistical validators in protein X-ray crystallography. *Acta. Crystallogr. D* **52**, 228–234 (1996).
57. Laskowski, R. A., MacArthur, M. W., Moss, D. S. & Thornton, J. M. *PROCHECK*: a program to check the stereochemical quality of protein structures. *J. Appl. Cryst.* **26**, 283–291 (1993).
58. Delano, W. L. *The PyMOL Molecular Graphics System*. v.0.99 (Delano Scientific, 2006).